Inorganic Chemistry

Article

pubs.acs.org/IC

Novel Coordination Frameworks Incorporating the 4,4′-Bipyrazolyl Ditopic Ligand

Claudio Pettinari,*[,†] Aurel Tăbăcaru,[†] Ishtvan Boldog,[‡] Konstantin V. Domasevitch,[‡] Simona Galli,*[,§] and Norberto Masciocchi[§]

[†]Scuola di Scienze del Farmaco e dei Prodotti della Salute, via S. Agostino 1, 62032 Camerino, Italy

[‡]National Taras Shevchenko University of Kyiv, Volodimirska Strasse 64, 01033 Kyiv, Ukraine

[§]Dipartimento di Scienza e Alta Tecnologia, Università dell'Insubria, via Valleggio 11, 22100 Como, Italy

Supporting Information

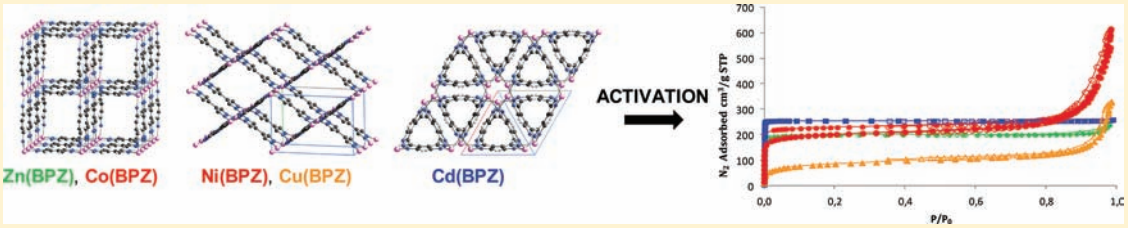

ABSTRACT: The reaction of the rigid spacer 4,4′-bipyrazole (H_2BPZ) with late transition metals, either following conventional routes or under solvothermal conditions, afforded the coordination polymers [M(BPZ)]·Solv (M = Zn, **1**; Co, **2**; Cd, **3**; Hg, **4**; Cu, **5**; Ni, **6**; Pd, **7**; Solv = DMF, **3**; MeCN, **5** and **6**; H_2O, **7**), $[Cu(H_2BPZ)_2(NO_3)_2]$ (**8**), and $[Cd(H_2BPZ)(CH_3COO)_2]$ (**9**). State-of-the-art laboratory powder diffraction methods allowed to disclose the isomorphous character of **1** and **2**, as well as of **5** and **6**, which feature 3D porous networks containing 1D channels of square and rhombic shape, respectively. **3**, crystallizing in the relatively rare $P6_122$ space group, consists of homochiral helices of octahedral Cd^{II} ions, packing in bundles mutually linked by "radial", nonplanar BPZ ligands. Finally, the dense species **8** and **9** contain parallel 2D layers of square and rectangular meshes, respectively. Thermogravimetric analyses witnessed the relevant thermal robustness of all the [M(BPZ)] materials [except the mercury(II) derivative], which are stable in air at least up to 300 °C, with the zinc(II) derivative decomposing only around 450 °C. Variable-temperature powder diffraction experiments highlighted the permanent porosity of **1**−**3**, **5**, and **6**, retained along consecutive temperature cycles in all cases but **3**. When probed with N_2 at 77 K, **1**−**3** and **5**−**7** showed Brunauer−Emmett−Teller and Langmuir specific surface areas in the ranges 314(2)−993(11) and 509(16)−1105(1) m^2/g, respectively.

1. INTRODUCTION

Coordination polymers[1] constitute a consolidated research topic in many different disciplines, ranging from inorganic chemistry to materials science and pharmacology. Because of the relevant functional properties they possess, such as magnetism,[2] luminescence,[3] and electric conductivity,[4] they find potential applications in numerous, technologically relevant fields.

When displaying permanent porosity, they constitute the most promising alternative to classic, natural or synthetic porous materials in key applications with energetic, environmental, and industrial fallout: the classic applications of storage[5] and separation[6] of gases or volatile organic compounds have been joined by the more recent ones of heterogeneous catalysis,[7] drug delivery, and imaging.[8] Porous coordination polymers (PCPs) rarely display thermal and chemical stabilities comparable to those of natural clays, synthetic zeolites, or activated carbons. Nevertheless, the careful choice of the metal ions, paying attention to their coordination number and stereochemistry, and of the organic spacers, modulating their size, shape, and steric hindrance, allows the engineering of PCPs with tuned topologies, pore sizes, and pore-window decorations. This advantage is further improved by the chemical (pre-[9] or postsynthetic[10]) modifications that can be carried out on the organic ligands.

Through the years, many cornerstone PCPs have been constructed, employing O-donor ligands as spacers. The renowned materials MOF-5,[11] MOF-177,[12] MIL-53,[13] and MIL-101[14] are just a few representative examples in this sense. Nevertheless, it was later demonstrated by us and by other research groups[9a,15] that N-donor ligands, in which N-based heterocyclic rings are bridged by rigid or partially flexible aromatic cores, provide metal−ligand coordinative bonds that are more stable and less subject to hydrolysis than their O-donor counterparts.[16] Thus, in polyazolato-based PCPs, key structural topologies are typically coupled to high thermal and chemical stabilities. The search for N-donor spacers conferring higher and higher robustness to PCPs has highlighted that pyrazolates normally surpass the imidazolate-, triazolate-, and

Received: January 19, 2012
Published: April 18, 2012

   dx.doi.org/10.1021/ic3001416 | *Inorg. Chem.* 2012, 51, 5235−5245

tetrazolate-based analogues, reaching decomposition temperatures, in air, above 400 °C.[17]

The coordination chemistry of the ditopic ligand 4,4′-bipyrazole (H_2BPZ; Scheme 1) has been recently investigated.

Scheme 1. 4,4′-Bispyrazole (H_2BPZ)

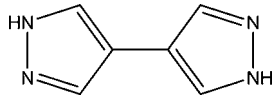

Only a few articles have appeared on the subject, dealing with transition-metal derivatives containing the neutral H_2BPZ moiety and showing polymeric crystal structures with different dimensionalities and motifs. The 1D chain $[Cu(H_2BPZ)(H_2O)_3(SO_4)]\cdot H_2O$, the 2D net $[Co(H_2BPZ)_2Cl_2]$, and the 3D network $[Cd(H_2BPZ)_2(NO_3)_2]$ are representative examples of the coordination chemistry of the neutral ligand.[18] The coordination ability of the corresponding dianion is exemplified by the work of Sun et al., who reported that dipalladium(II,II) and diplatinum(II,II) clips can be bridged by BPZ to give metallomacrocycles with interesting photophysical properties.[19]

Our long-term experience with polyazolato-based coordination polymers[15a,17c−e,20] prompted us to further exploit the coordinative potentialities of the H_2BPZ spacer toward transition-metal ions, in the search for thermally robust, functional coordination polymers. Hereafter, we report on the synthesis as well as on the spectroscopic, thermal, and structural characterization of two classes of coordination polymers, isolated by reacting H_2BPZ with a set of late transition metal ions. In particular, 3D PCPs containing the BPZ dianion could be prepared either in a "conventional" environment, in the presence of a deprotonating agent, or following a solvothermal route. Their permanent porosity, witnessed by variable-temperature X-ray powder diffraction (TXRPD) experiments, was essayed toward N_2 at 77 K. On the contrary, the absence of a deprotonating agent along a conventional synthetic path led to the isolation of H_2BPZ-containing derivatives, featuring 2D slabs in which the metal coordination environment is completed by the counterions.

2. EXPERIMENTAL SECTION

2.1. Materials and Methods. 4,4′-Bipyrazole (H_2BPZ) was synthesized by following the method reported in the literature.[18] All of the chemicals and reagents used were purchased from Sigma Aldrich Co. and used as received without further purification. All of the solvents were distilled prior to use. IR spectra were recorded from 4000 to 650 cm^{-1} with a Perkin-Elmer Spectrum 100 instrument by total reflectance on a CdSe crystal. Elemental analyses (C, H, and N) were performed with a Fisons Instruments 1108 CHNS-O elemental analyzer. Thermogravimetric analyses (TGA) were carried out in a N_2 stream with a Perkin-Elmer STA 6000 simultaneous thermal analyzer with heating rates in the range 5−10 °C/min.

2.2. Synthesis of [Zn(BPZ)] (1). H_2BPZ (0.0268 g, 0.2 mmol) was dissolved in 30 mL of methanol. Then, 2 equiv of sodium methoxide (0.0216 g, 0.4 mmol) was added. After $^1/_2$ h of gentle warming at 45 °C with concomitant stirring, $Zn(CH_3COO)_2\cdot 2H_2O$ (0.0439 g, 0.2 mmol) was added. The solution was left under stirring at room temperature for 24 h. A white precipitate was obtained, filtered off, washed twice with methanol, and dried in vacuo. Yield: 70%. **1** is insoluble in alcohols, dimethyl sulfoxide (DMSO), acetone, CH_3CN, chlorinated solvents, and water. Elem anal. Calcd for $C_6H_4N_4Zn$ (fw = 197.5 g/mol): C, 36.49; H, 2.04; N, 28.37. Found: C, 36.16; H, 1.94; N, 27.96. IR (cm^{-1}): 3102(vw) [ν(C−$H_{aromatic}$)]; 1521(s) [ν(C═C + C═N)]; 1389(s), 1296(w), 1268(s), 1171(m), 1161(m), 1052(s), 1015(w), 919(s), 833(s). **1** may be isolated also by using different ZnX_2 salts (X = HCOO, CF_3COO, CF_3SO_3, or ClO_4).

2.3. Synthesis of [Co(BPZ)] (2). H_2BPZ (0.067 g, 0.5 mmol) was dissolved in 15 mL of dimethylformamide (DMF). Then, $Co(CH_3COO)_2\cdot 4H_2O$ (0.1245 g, 0.5 mmol) was added. The mixture was left under stirring in a high-pressure glass tube at 120 °C for 24 h, until a violet precipitate appeared and was filtered off, washed with hot dichloromethane, and dried in vacuo. Yield: 75%. **2** is insoluble in alcohols, DMSO, acetone, CH_3CN, chlorinated solvents, and water. Elem anal. Calcd for $C_6H_4CoN_4$ (fw = 191.1 g/mol): C, 37.33; H, 2.11; N, 29.32. Found: C, 37.22; H, 2.14; N, 29.36. IR (cm^{-1}): 3102(vw) [ν(C−$H_{aromatic}$)]; 1516(s) [ν(C═C + C═N)]; 1383(s), 1260(s), 1165(sh), 1156(m), 1046(s), 1014(w), 917(m), 831(m), 659(br).

2.4. Synthesis of [Cd(BPZ)]·DMF (3). H_2BPZ (0.067 g, 0.5 mmol) was dissolved in 15 mL of DMF. Then, $Cd(NO_3)_2\cdot 4H_2O$ (0.154 g, 0.5 mmol) was added in small portions. The mixture was left under stirring in a high-pressure glass tube at 150 °C for 24 h, until a white precipitate formed and was filtered off, washed with 20 mL of dichloromethane, and dried in vacuo. Yield: 86%. **3** is insoluble in alcohols, DMSO, acetone, CH_3CN, chlorinated solvents, and water. Elem anal. Calcd for $C_9H_{11}CdN_5O$ (fw = 317.6 g/mol): C, 34.02; H, 3.49; N, 22.05. Found: C, 33.70; H, 3.27; N, 21.66. IR (cm^{-1}): 3121(ww) [ν(C−$H_{aromatic}$)]; 2927(vw) [ν(C−$H_{aliphatic}$)]; 1645(vs) [ν(C═O)]; 1507(w) [ν(C═C + C═N)]; 1378(m), 1252(s), 1151(m), 1099(m), 1040(m), 995(w), 918(s), 826(m), 816(sh), 809(w), 658(m).

2.5. Synthesis of [Hg(BPZ)] (4). H_2BPZ (0.0134 g, 0.1 mmol) was dissolved in 30 mL of acetonitrile. After gentle warming at 45 °C for 15 min with concomitant stirring, $Hg(CH_3COO)_2$ (0.0318 g, 0.1 mmol) was added. Then, the solution was stirred under reflux for 10 h. A white precipitate formed and was filtered off, washed with acetonitrile (2 × 10 mL), and dried in vacuo. Yield: 83%. **4** is insoluble in alcohols, DMSO, acetone, CH_3CN, chlorinated solvents, and water. Elem anal. Calcd for $C_6H_4HgN_4$ (fw = 332.7 g/mol): C, 21.66; H, 1.21; N, 16.84. Found: C, 21.95; H, 1.29; N, 16.67. IR (cm^{-1}): 3134(w) [ν(C−$H_{aromatic}$)]; 1630(w), 1508(w) [ν(C═N + C═C)]; 1406(br), 1375(m), 1310(w), 1292(w), 1252(m), 1166(s), 1149(m), 1046(s), 971(m), 913(m), 860(s), 815(s), 661(s).

2.6. Synthesis of [Cu(BPZ)]·MeCN (5). H_2BPZ (0.0268 g, 0.2 mmol) was dissolved in 30 mL of acetonitrile. After gentle warming at 45 °C for 15 min with concomitant stirring, $Cu(CH_3COO)_2$ (0.0363 g, 0.2 mmol) was added in small portions. Then, the solution was stirred at room temperature for 24 h, until a brownish precipitate formed, which was filtered off, washed with acetonitrile (2 × 10 mL), and dried in vacuo. Yield: 85%. **5** is insoluble in alcohols, DMSO, acetone, CH_3CN, chlorinated solvents, and water. Elem anal. Calcd for $C_8H_7CuN_5$ (fw = 236.7 g/mol): C, 40.59; H, 2.98; N, 29.58. Found: C, 40.15; H, 2.82; N, 29.73. IR (cm^{-1}): 3107(vw) [ν(C−$H_{aromatic}$)]; 2929(w) [ν($CH_{aliphatic}$)]; 2250(w) [ν(C≡N)]; 1579(br), 1509(vs) [ν(C═C + C═N)]; 1391(s), 1361(w), 1332(w), 1266(s), 1177(m), 1161(m), 1057(s), 1012(w), 921(s), 832(s). For the sake of completeness, we add here that the solvothermal reaction of $Cu(CH_3COO)_2$ with H_2BPZ at 120 °C for 2 h leads to the recovery of an amorphous desolvated form of **5**.

2.7. Synthesis of [Ni(BPZ)]·MeCN (6). To a solution of $Ni(CH_3COO)_2\cdot 4H_2O$ (0.084 g, 0.47 mmol) in 10 mL of acetonitrile H_2BPZ (0.089 g, 0.47 mmol) was added in one single portion with stirring. The mixture was stirred at 60 °C for 10 min, and then 1 mL of triethylamine was added. The reaction was kept under reflux for 8 h. The dark-orange precipitate formed was filtered off, washed with acetonitrile, and dried in vacuo. IR spectroscopy indicated the presence of unreacted ligand in the isolated precipitate, which was further washed by suspending it in DMSO (10 mL) at 60 °C. The DMSO-washed batch was dried in vacuo at 140 °C for 4 h to afford the final product. Yield: 77%. **6** is soluble in DMSO and insoluble in alcohols, acetone, CH_3CN, chlorinated solvents, and water. Elem anal. Calcd for $C_8H_7N_5Ni$ (fw = 231.9 g/mol): C, 41.44; H, 3.04; N, 30.20. Found: C, 40.91; H, 3.05; N, 30.12. IR (cm^{-1}): 3101(vw) [ν(C−$H_{aromatic}$)]; 2939(w) [ν(C−$H_{aliphatic}$)]; 2250(w) [ν(C≡N)]; 1631(w),

dx.doi.org/10.1021/ic3001416 | Inorg. Chem. 2012, 51, 5235−5245

Table 1. Crystal Data and Refinement Details for Compounds 1, 3, 5, 6, 8, and 9

	1	3	5	6	8	9
empirical formula	$C_6H_4N_4Zn$	$C_9H_{11}CdN_5O$	$C_8H_7CuN_5$	$C_8H_7N_5Ni$	$C_{12}H_{12}CuN_{10}O_6$	$C_{10}H_{12}CdN_4O_4$
fw, g/mol	197.51	317.63	236.72	231.87	455.82	364.64
cryst syst	tetragonal	hexagonal	orthorhombic	orthorhombic	monoclinic	triclinic
space group, Z	$P4_2/mmc$, 2	$P6_122$, 6	$Imma$, 4	$Imma$, 4	$P2_1/n$, 2	$P\bar{1}$, 1
a, Å	8.831(2)	10.0903(1)	15.789(1)	14.660(2)	8.2385(4)	4.97710(2)
b, Å	8.831(2)	10.0903(1)	7.1328(6)	6.9494(7)	13.3121(6)	7.2240(3)
c, Å	7.301(2)	21.2568(4)	8.7207(6)	10.024(1)	8.0524(5)	10.7903(6)
α, deg	90	90	90	90	90	112.954(2)
β, deg	90	90	90	90	112.333(3)	97.900(3)
γ, deg	90	120	90	90	90	70.137(3)
V, Å^3	569.4(3)	1874.29(6)	982.1(1)	1021.2(2)	816.88(8)	337.33(3)
ρ_{calcd}, g/cm^3	1.153	1.688	1.601	1.508	1.845	1.785
$F(000)$	196	936	476	472	458	180
μ(Cu Kα), cm^{-1}	26.5	139.0	28.7	24.9	24.8	131.8
T, K	298(2)	298(2)	298(2)	298(2)	298(2)	298(2)
refinement 2θ range, deg	8−105	9−105	10−105	7−105	12.5−105	8−105
N_{data}	4851	4801	4501	4901	4626	4851
R_p, R_{wp}[a]	0.081, 0.114	0.053,0.073	0.043, 0.066	0.014,0.022	0.030, 0.046	0.054, 0.070
R_{Bragg}[a]	0.052	0.038	0.059	0.008	0.019	0.036

[a] $R_p = \sum_i|y_{i,o} - y_{i,c}|/\sum_i|y_{i,o}|$; $R_{wp} = [\sum_i w_i(y_{i,o} - y_{i,c})^2/\sum_i w_i(y_{i,o})^2]^{1/2}$; $R_{Bragg} = \sum_n|I_{n,o} - I_{n,c}|/\sum_n I_{n,o}$, where $y_{i,o}$ and $y_{i,c}$ are the observed and calculated profile intensities, respectively, while $I_{n,o}$ and $I_{n,c}$ are the observed and calculated intensities. The summations run over i data points or n independent reflections. Statistical weights w_i are normally taken as $1/y_{i,o}$.

1511(w) [ν(C═C + C═N)]; 1400(s), 1284(sh), 1275(s), 1186(m), 1165(s), 1062(s), 921(s), 818(s). For the sake of completeness, we add here that the solvothermal reaction of $Ni(CH_3COO)_2{\cdot}4H_2O$ with H_2BPZ at 120 °C for 2 h leads to the recovery of an amorphous desolvated form of **6**.

2.8. Synthesis of [Pd(BPZ)]·H$_2$O (7). H_2BPZ (0.067 g, 0.5 mmol) was dissolved in 15 mL of DMF. Then, $Pd(CH_3COO)_2{\cdot}H_2O$ (0.121 g, 0.5 mmol) was added. The mixture was stirred in a high-pressure glass tube at 120 °C for 24 h. A dark-green precipitate formed and was filtered off, washed with 20 mL of dichloromethane, and dried in vacuo. Yield: 75%. **7** is insoluble in alcohols, DMSO, acetone, CH_3CN, chlorinated solvents, and water. Elem anal. Calcd for $C_6H_6PdN_4O$ (fw = 256.6 g/mol): C, 28.09; H, 2.36; N, 21.84. Found: C, 29.13; H, 2.39; N, 21.54. IR (cm^{-1}): 3400−3200(br) [ν(O−H)]; 3123(w) [ν(C−H$_{aromatic}$)]; 1640(sb), 1624(br) [ν(O−H)]; 1510(s) [ν(C═C + C═N)]; 1388(s), 1330(m), 1277(m), 1169(s), 1054(s), 915(s), 825(s br), 752(s).

2.9. Synthesis of [Cu(H$_2$BPZ)$_2$(NO$_3$)$_2$] (8). H_2BPZ (0.0268 g, 0.2 mmol) was dissolved in 30 mL of methanol. After gentle warming at 45 °C for 15 min with concomitant stirring, $Cu(NO_3)_2{\cdot}2.5H_2O$ (0.0468 g, 0.2 mmol) was added. The solution was stirred at room temperature for 24 h. A green precipitate immediately formed, which turned to violet-bluish in 12 h, reasonably because of a change in the stereochemistry of the metallic center.[21] The bluish precipitate was filtered off, washed with methanol (2 × 20 mL), and dried in vacuo. Yield: 80%. **8** is soluble in DMSO and insoluble in alcohols, acetone, CH_3CN, chlorinated solvents, and water. Elem anal. Calcd for $C_{12}H_{12}CuN_{10}O_6$ (fw = 455.84 g/mol): C, 31.62; H, 2.65; N, 30.73. Found: C, 31.23; H, 2.45; N, 30.58. IR (cm^{-1}): 3341(m) [ν(N−H)]; 3131(w), 3117(w) [ν(C−H$_{aromatic}$)]; 1548(m), 1520(m) [ν(C═C + C═N)]; 1407(vs) [ν_{asim}(NO$_3$)]; 1375(m), 1307(vs) [ν_{sim}(NO$_3$)]; 1233(m), 1170(m), 1120(s), 1046(s), 971(s), 913(m), 853(s), 820(m), 768(m br), 717(s), 704(s).

2.10. Synthesis of [Cd(H$_2$BPZ)(CH$_3$COO)$_2$] (9). H_2BPZ (0.0268 g, 0.2 mmol) was dissolved in 30 mL of methanol. After gentle warming at 50 °C for 15 min with concomitant stirring, $Cd(CH_3COO)_2{\cdot}2H_2O$ (0.0533 g, 0.2 mmol) was added. The solution was stirred at room temperature for 24 h. A white precipitate formed and was filtered off, washed with methanol (2 × 15 mL), and dried in vacuo. Yield: 80%. **9** is insoluble in alcohols, DMSO, acetone, CH_3CN, chlorinated solvents, and water. Elem anal. Calcd for $C_{10}H_{12}CdN_4O_4$ (fw = 364.64 g/mol): C, 32.94; H, 3.32; N, 15.36. Found: C, 32.82; H, 3.22; N, 14.99. IR (cm^{-1}): 3310(m) [ν(N−H)]; 3125(w) [ν(C−H$_{aromatic}$)]; 2972(w) [ν(C−H$_{aliphatic}$)]; 1557(vs) [ν_{asim}(COO)]; 1472(w), 1410(s), 1385(vs) [ν_{sim}(COO)]; 1342(m), 1320(w), 1306(w), 1260(s), 1165(s), 1151(m), 1141(m), 1045(s), 1013(w), 999(w), 958(s), 934(w), 920(m), 867(m), 836(m), 720(s).

2.11. X-ray Powder Diffraction (XRPD) Crystal Structures Determination. Batches of compounds **1**−**9** were gently ground in an agate mortar; then, they were deposited in the hollow of an aluminum sample holder equipped with a zero-background plate. Diffraction data were collected at room temperature on a Bruker AXS D8 Advance diffractometer, equipped with Ni-filtered Cu Kα radiation (λ = 1.5418 Å), a Lynxeye linear position-sensitive detector, and the following optics: primary beam Soller slits (2.3°), fixed divergence slit (0.5°), receiving slit (8 mm). The generator was set at 40 kV and 40 mA. The nominal resolution for the present setup is 0.08° of 2θ (FWHM of the α_1 component) for the LaB_6 peak at about 2θ = 21.3°. Preliminary acquisitions revealed that compounds **1**−**3**, **5**, **6**, **8**, and **9** are polycrystalline; on the contrary, the diffraction traces of **4** and **7** feature only broad peaks or even halos, typical of nearly amorphous materials. Different synthetic attempts did not allow to recover crystalline materials: thus, the structural features of **4** and **7** remain presently unknown. A visual inspection of the diffractograms of **1** and **2** and of **5** and **6** allowed to purport their isomorphism. Because of the experimental setup, lacking a monochromator on the diffracted beam, the XRPD pattern of **2** is deeply affected by fluorescence, hampering the full (statistically significant) structure solution and refinement. For all of the remaining polycrystalline species, overnight scans were performed in the 2θ range of 5−105°, with 0.02° steps. A standard peak search, followed by indexing of the first peaks (2θ < 30°) through the single value decomposition approach[22] implemented in TOPAS-R,[23] allowed the determination of the lattice parameters. Systematic absences, the above-mentioned isomorphism, and geometrical considerations allowed to individuate the most probable space groups. Successful Le Bail refinements confirmed the unit cells and space groups. The structural models employed in the final whole-pattern Rietveld refinements were determined ab initio by the simulated annealing technique as implemented in TOPAS-R; for the crystallographically independent portion of the ligand, an idealized rigid model was used,[24] in which the torsion angle around the C−C single bond was allowed to refine when pertinent. When present, also counterions

dx.doi.org/10.1021/ic3001416 | Inorg. Chem. 2012, 51, 5235−5245

and solvent molecules were described by rigid models. The peak shapes were described by the fundamental parameters approach.[25] In the case of **1**, **3**, **5**, and **6**, the anisotropic broadening of the peaks was modeled by means of spherical harmonics. This model alone is not enough in the case of **1** because of the very high anisotropy of its peaks. A different approach, modeling paracrystallinity, is presently under development. The background was modeled by a Chebyshev polynomial function. The thermal effect was simulated by using a single isotropic parameter for the metal ions, augmented by 2.0 $Å^2$ for lighter atoms. Table 1 contains the relevant crystallochemical data and structure refinement details. The final Rietveld refinement plots are collectively supplied in Figures S1 and S2 in the Supporting Information. Fractional atomic coordinates are supplied in the Supporting Information as CIF files. X-ray crystallographic data in CIF format have been deposited at the Cambridge Crystallographic Data Center as supplementary publications CCDC 863371−863376. Copies of the data can be obtained free of charge upon application to the Director, CCDC, 12 Union Road, Cambridge CB2 1EZ, U.K. (fax +44-1223-335033; e-mail deposit@ccdc.cam.ac.uk, or weblink http://www.ccdc.cam.ac.uk).

2.12. Variable-Temperature X-ray Powder Diffraction (TXRPD). TXRPD experiments were performed on the as-synthesized species **1**−**3**, **5**, and **6** to highlight their "structural" response to temperature variations (here intended as cycles of heating and successive cooling to room temperature). The experiments were carried out in air using a custom-made sample heater, assembled by Officina Elettrotecnica di Tenno, Ponte Arche, Italy. Powdered microcrystalline samples of the materials were ground in an agate mortar and deposited in the hollow of an aluminum sample holder. The TXRPD cycles were performed in air, in a significant low-angle 2θ range, heating or cooling in situ in a temperature range mainly dictated by the specific characteristics of the single material. For **1** and **2**, whose as-synthesized batches do not contain clathrated solvent, the cycles were performed in the range 30−130 °C, increasing or decreasing the temperature by 20 °C/step. Faster cycles in the range 30−200 °C (the temperature of evacuation before performing the N_2 adsorption measurements being 200 °C; see section 2.13) were also carried out. For **3** and for **5** and **6**, containing DMF and acetonitrile, the cycles were carried out in the ranges 30−240 and 30−210 °C, respectively. Parametric treatment of the acquired data with the Le Bail method allowed to depict the unit cell parameters variation as a function of the temperature.[26] When comparing the TGA and TXRPD results, the reader must be aware that the thermocouple of the TXRPD setup is *not* in direct contact with the sample, this determining a slight difference in the temperature at which the same event is detected by the two techniques. The TGA temperatures have to be considered as more reliable.

2.13. Gas Sorption Measurements. Gas sorption isotherms for pressures in the range 0−1 bar were measured by the volumetric method using a Beckman Coulter SA 3100 surface area and pore size analyzer instrument, adopting the following procedure. A sample of ca. 50 mg of the as-synthesized material was introduced into a preweighed analysis tube (9 mm diameter; 9 cm^3 bulb), capped with a gastight TranSeal to prevent the intrusion of oxygen and atmosphere moisture during transfer and weighing. Samples of species **1**−**3** and **5**−**7** were evacuated under dynamic vacuum (ca. 10^{-5} bar) at 200 °C, until a constant weight was achieved. Because of its lower decomposition temperature, **4** was activated, following the same procedure, at 120 °C. The analysis tube was then transferred to an electronic balance and weighed again to determine the mass of the sample. Finally, it was transferred to the analysis port of the gas sorption instrument. For all isotherms, warm and cold free-space correction measurements were performed using ultrahigh-purity (UHP) helium gas (UHP grade 5.0, 99.999% purity); N_2 isotherms were measured at 77 K in a liquid-nitrogen bath using UHP-grade gas sources.

3. RESULTS AND DISCUSSION

3.1. Synthesis and Spectroscopic Characterization of the BPZ-Containing Species 1−7. For all of the probed metal ions, isolation of coordination compounds of the [M(BPZ)]·Solv type, containing the BPZ dianion, requires either a "conventional" synthetic route in the presence of a base or application of solvothermal conditions.

Indeed, **1** can be obtained by a conventional path by reacting ZnX_2 salts (X = CH_3COO, HCOO, CF_3COO, CF_3SO_3, or ClO_4) and H_2BPZ in methanol, in the presence of a base. The latter is required, irrespectively of the metal salt employed, in order to recover a pure product. The mercury(II), copper(II), and nickel(II) derivatives **4**−**6** can be prepared from the corresponding acetates following similar synthetic conditions but employing MeCN as the solvent. Only in the case of nickel(II) must the starting system be treated at reflux to induce precipitation of the product. On the contrary, **2**, **3**, and **7** precipitate when cobalt(II), cadmium(II), and palladium(II) acetates, respectively, are treated with H_2BPZ in DMF, in a high-pressure glass tube at 120 °C. In these three cases, ligand deprotonation does not require an external deprotonating agent.

All of the isolated species precipitate in high yields in the form of air-stable powders insoluble in the most common organic solvents, this evidence suggesting their polymeric nature. As a matter of fact, the absence of N−H stretching bands in their IR spectra indicates the formation of metal-bridging polypyrazolate dianions. IR spectroscopy also confirms the presence of trapped solvent molecules: in the spectrum of **3**, the band centered at 1640 cm^{-1} can be interpreted as the C═O stretching of DMF;[27] in the spectra of **5** and **6**, the band centered at 2250 cm^{-1} is due to the C≡N stretching vibration of CH_3CN. As expected, the observations emerging from the spectroscopic investigations were successfully confirmed by the structural studies.

3.2. Synthesis and Spectroscopic Characterization of the H_2BPZ-Containing Species 8 and 9. The role of an external deprotonating agent along a conventional route is evident when copper(II) nitrate and cadmium(II) acetate are treated with H_2BPZ in methanol, at room temperature: in the absence of a base, **8** and **9** are isolated.

The two species are recovered as polycrystalline powdered solids, stable in air and insoluble in the most common organic solvents, suggesting their polymeric nature. As expected, in their IR spectra, a strong absorption band can be detected because of the N−H vibration of the neutral H_2BPZ ligand (3341 cm^{-1} in both cases). In addition, in the spectrum of **8**, the asymmetric and symmetric stretching modes of the nitrate anion can be recognized at 1407−1375 and 1307 cm^{-1}, respectively; they are accompanied by two very weak signals at 1750−1760 cm^{-1}, overtones of nitrate ions exhibiting a monodentate coordination mode.[28] In the spectrum of **9**, the two strong bands at 1557 and 1410−1385 cm^{-1} correspond to the asymmetric (ν_a) and symmetric (ν_s) stretching modes of the acetate anion, respectively. Their difference, $\Delta\nu = \nu_a - \nu_s$ = 147÷172 cm^{-1}, likely indicates a bridging coordination geometry.[29] For both species, the polymeric nature of the crystal structure and the coordination modes of the counterions suggested by IR spectroscopy were confirmed by the structural studies.

3.3. Structural Analysis of the BPZ-Containing Species 1−3, 5, and 6. The crystal and molecular structures discussed hereafter have been retrieved from state-of-the-art structural XRPD methods.[30]

1 and **2**, containing divalent metal ions with the same stereochemical preferences, are isomorphous. As anticipated in

dx.doi.org/10.1021/ic3001416 | Inorg. Chem. 2012, 51, 5235−5245

the Experimental Section, the high fluorescence contaminating the XRPD trace of **2** hampered its complete structural characterization. Thus, only the structural features of **1** will be discussed in detail.

1 crystallizes in the tetragonal space group $P4_2/mmc$. The asymmetric unit contains one Zn^{II} ion and one ligand, both lying about high-symmetry sites ($\bar{4}m2$ and *mmm*, respectively). The Zn^{II} ions are coordinated, within tetrahedral stereochemistry, by four N atoms of four exo-tetradentate BPZ ligands (Figure 1, inset). The ligands bridge consecutive metal ions, thus forming 1D linear chains running parallel to the crystallographic axis *c*. The chains are further bridged by the BPZ spacers along *a* and *b*, which promotes the formation of a 3D framework. Within the latter, the reciprocal disposition of metal ions and bridging ligands is responsible for the presence of 1D square-shaped channels running along *c*, of which the ligands constitute the walls (Figure 1). The overall crystal structure of **1** recalls that of its larger analogue [Zn(BDP)] (H_2BDP = bipyrazolyl-1,4-benzene), a cornerstone in the realm of polyazolate-based PCPs for its high thermal inertness and its capability of separating volatile organic compounds with similar boiling points (e.g., benzene and cyclohexane).[17d] **1** and [Zn(BDP)] represent a successful example of the so-called isoreticular approach, originally introduced by Yaghi et al.:[31] while the framework topology is preserved, the pore size and decoration may be systematically varied upon modification of the length and substitution of the spacers. As a matter of fact, the different sizes of the two organic spacers (reflected by the length of *a*, 8.83 and 13.27 Å, in **1** and [Zn(BDP)], respectively) result in different void volumes, which, as predicted, are significantly lower in **1** (42%[32] vs 65% in [Zn(BDP)]).

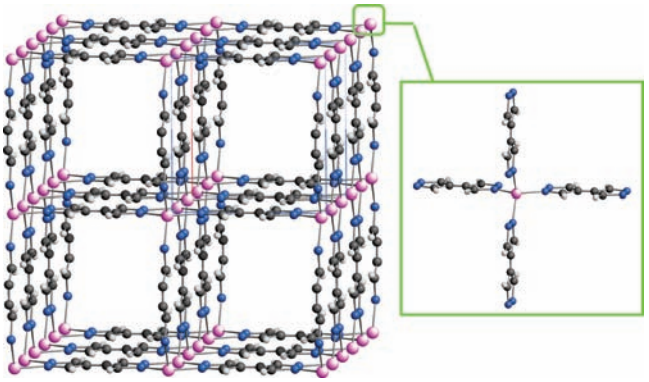

Figure 1. Portion of the crystal packing of species **1**, [Zn(BPZ)], highlighting the 1D square channels running along the crystallographic axis *c*. The tetrahedral coordination sphere of the metal ions can be appreciated in the inset. Color code: Zn, purple; N, blue; C, gray; H, light gray. Significant bond distances (Å) and angles (deg): Zn−N, 2.122(5); Zn···Zn, 3.645(1); N−Zn−N, 106.93(9)−114.7(2).

When the BPZ spacer is coupled to divalent metal ions typically adopting square-planar stereochemistry, porous 3D networks differing in the shape of the 1D channels are expected, as was the case with [Ni(BDP)], whose flexible channels trap harmful organics like tetrahydrothiophene, also in the presence of humidity.[17d] **5** and **6**, containing Cu^{II} and Ni^{II} ions, respectively, conform to this stereochemical rule, confirming once more the viability of the isoreticular approach. Indeed, as Ni(BDP), also **5** and **6** crystallize in the orthorhombic space group *Imma*. The asymmetric unit contains one metal ion and one ligand, both lying on special positions (2/*m* and *mm*2, respectively). The metal ions are coordinated, within square-planar stereochemistry, by four N atoms of four exo-tetradentate BPZ ligands (Figure 2). The ligands bridge consecutive metal ions along 1D linear chains running parallel to the crystallographic axis *b*. The chains are further bridged by the BPZ spacers along the (101) and (10−1) planes, which brings about the formation of a 3D framework. The latter features 1D, rhombus-shaped channels running along *b* (Figure 2). The two materials differ in the disposition of the solvent molecules characterizing the as-synthesized specimens. In **5**, the coordination sphere of the metal ions is completed by two coordinative bonds with two CH_3CN molecules, which occupy the apical positions of a Jahn−Teller elongated CuN_6 octahedron (Figure 2a), in the same way as that with DMF in the isomorphous species [Cu(BDT)(DMF)][33] and [Cu(BDTri)(DMF)]·1.2H_2O[34] [H_2BDT = 1,4-benzeneditetrazole; H_2BDTri = 1,4-benzenedi(1*H*-1,2,3-triazole)]. Differently, in **6**, where the Ni^{II} ions are more satisfactorily set in a square-planar arrangement, the acetonitrile molecules are hosted in the channels, without being involved in bonding interactions with the metal ions (Figure 2b, where, for the sake of clarity, the solvent has been removed). The void volume is 40 and 42%,[32] for **5** and **6**, respectively. In line with that described above for

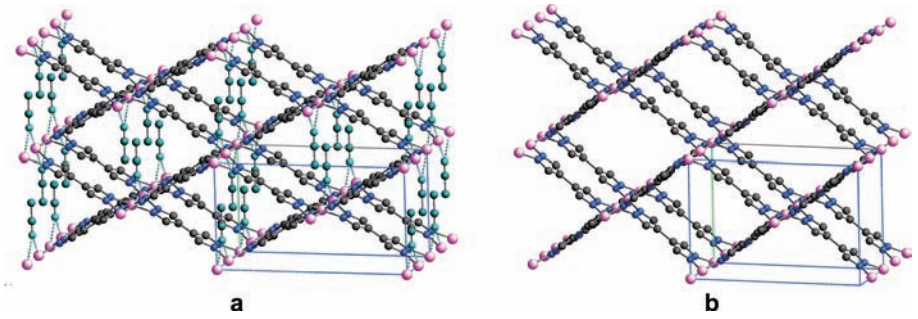

Figure 2. Portion of the crystal packing of (a) species **5**, [Cu(BPZ)]·CH_3CN, and (b) species **6**, [Ni(BPZ)]·CH_3CN, highlighting the 1D rhombic channels running along the crystallographic axis *b*. In **5**, the acetonitrile molecules (drawn in cyan) are weakly bound to the metal ions (fragmented lines). In **6**, they are hosted in the rhombic channels and have been removed for the sake of clarity. Horizontal axis: *a*. Vertical axis: *c*. Color code: Cu, purple; N, blue; C, gray. The H atoms have been omitted for clarity. Significant bond distances (Å) and angles (deg) for **5**: Cu−N, 2.012(3); Cu−$N_{acetonitrile}$, 2.713(9); Cu···Cu, 3.5669(3) Å; N−Cu−N, 86.3(4), 87.0(2), 93.7(4). Significant bond distances (Å) and angles (deg) for **6**: Ni−N, 1.84(2); Ni···Ni, 3.4747(4) Å; N−Ni−N, 87(2), 94(2).

dx.doi.org/10.1021/ic3001416 | *Inorg. Chem.* 2012, 51, 5235−5245

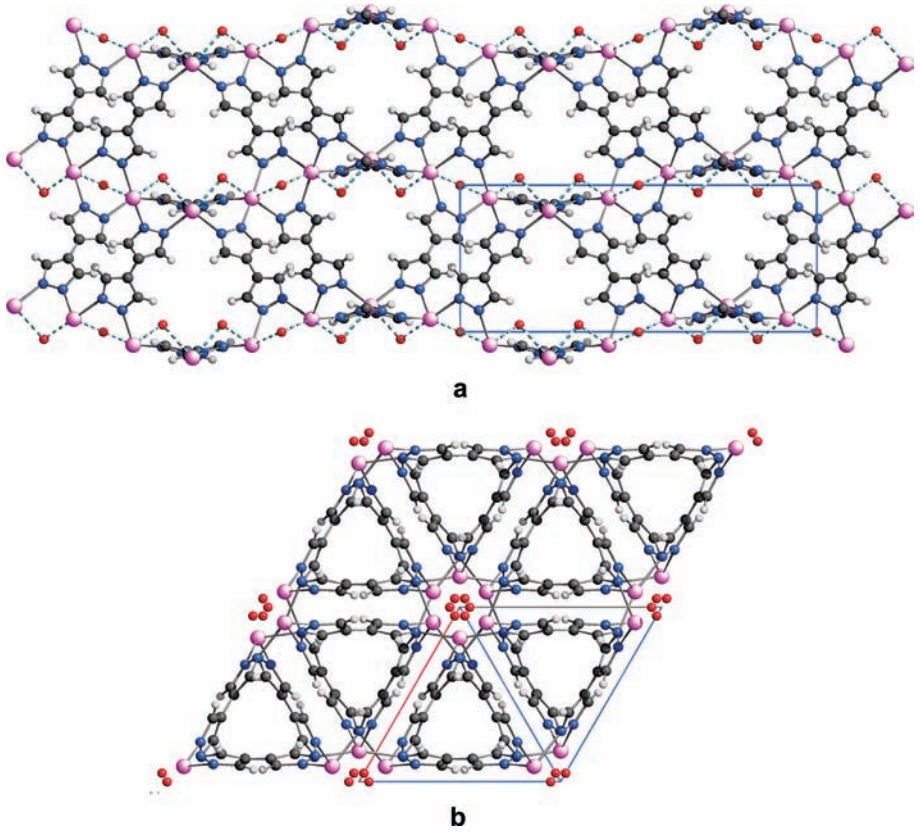

Figure 3. Portion of the crystal packing of species **3**, [Cd(BPZ)]·DMF, viewed down [100] (a) and [001] (b). Color code: Cd, purple; N, blue; O, red; C, gray; H, light gray. For the sake of simplicity, the disordered DMF molecules have been removed, leaving just their O atoms weakly bound to the Cd^{II} ions (fragmented lines). The helical motif of the metal centers, folding about a 6_1 axis, is evident from the wavy sequence of purple spheres along the horizontal axis *c* in part a. Significant bond distances (Å) and angles (deg): Cd−N, 2.27(2), 2.33(2); Cd−O, 2.665(8); Cd···Cd, 3.864(1); N−Cd−N, 91(2), 98(8), 108(8), 165(11); N−Cd−O, 79(4), 85(3), 90(5), 165(5); O−Cd−O, 84.3(3).

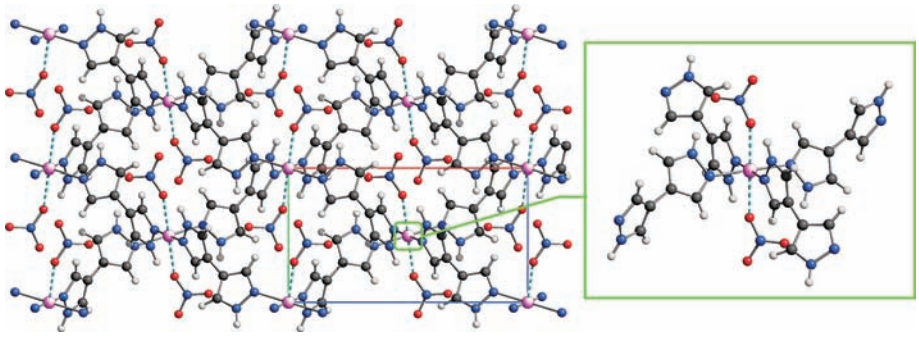

Figure 4. Portion of the crystal packing of species **8**, $[Cu(H_2BPZ)_2(NO_3)_2]$, viewed down [100]. The horizontal axis is *c*. Color code: Cu, purple; N, blue; O, red; C, gray; H, light gray. The octahedral coordination sphere of the metal ions can be better appreciated in the inset. The Cu−O long interactions are depicted with fragmented lines. Significant bond distances (Å) and angles (deg): Cu−N, 1.968(5), 2.096(5); Cu−O, 2.423(7); Cu···Cu, 9.4915(6); N−Cu−N, 88.6(3), 91.4(4); N−Cu−O, 84.2(3), 95.8(3).

the couple **1** and [Zn(BDP)], it is lower than the value of 57% estimated for [Ni(BDP)].

Surprisingly, the cadmium(II) derivative **3**, which was originally prepared to isolate a crystal phase isomorphous to **1** and **2**, crystallizes in the *significantly rare* hexagonal space group $P6_122$.[35] The asymmetric unit contains one metal ion, one ligand, and one DMF molecule, all lying in special positions (..2, .2., and .2., respectively). More in detail, the metal ions and BPZ spacers are bisected by crystallographic 2-fold axes, while the DMF molecules are disordered and manifest a lower molecular symmetry, yet maintaining the O-donor atoms on the symmetry element. The Cd^{II} ions possess a *cis*-O_2N_4 octahedral stereochemistry, defined by four N atoms of four BPZ ligands and by two O atoms of two DMF molecules. Each DMF molecule bridges two consecutive Cd^{II} ions, promoting the formation of 1D helical chains winding up a 6_1 (or 6_5, in the enantiomorphic crystals) screw axis (Figure 3). Approximately in the planes parallel to *ab*, the chains are bridged by the BPZ ligands, which results in the formation of a 3D network. Notably, the ligands show a significant twist (the torsion angle between the pyrazolato rings, ϕ, amounts to 30.2°), likely induced by the stereochemical constraints at the Cd^{II} ions and by the proximity of the homochiral Cd_n helices.

dx.doi.org/10.1021/ic3001416 | *Inorg. Chem.* 2012, 51, 5235−5245

Removal of the solvent molecules from the final structural model leaves 50% of the crystal volume unoccupied.[32]

3.4. Structural Analysis of the H_2BPZ-Containing Species 8 and 9. As confirmed by our XRPD studies, in the crystal structures of **8** and **9**, the pyrazole-based ligand is not deprotonated and acts as a μ_2,η^1,η^1 bridge.

Species **8** crystallizes in the monoclinic space group $P2_1/n$. The asymmetric unit contains one metal ion, lying on a crystallographic inversion center ($\bar{1}$ site), one H_2BPZ spacer, and one counterion, both in general positions. The metal ions are coordinated, within square-planar stereochemistry, by four N atoms of four BPZ spacers. The coordination environment of Cu^{II} is completed by two nitrates, axially bound through weak Cu−O interactions, generating octahedral *trans*-CuN_4O_2 units. Metal bridging by the BPZ spacers brings about the formation of 2D slabs of $[Cu(H_2BPZ)_2]_n$ formulation, lying in the (101) plane and featuring square meshes hinged at the CuN_4 nodes (Figure 4).

At variance, species **9** crystallizes in the triclinic space group $P\bar{1}$. The asymmetric unit contains one metal ion and one H_2BPZ spacer, lying on crystallographic inversion centers, and one counterion in a general position. The metal ions possess octahedral stereochemistry, defined by four N atoms of four BPZ spacers and by two counterions, occupying the apical positions and adopting a bridging coordination mode, in agreement with the evidence of IR spectroscopy. DMF bridging creates $[Cd(CH_3COO)_2]_n$ parallel chains running along *a*. The chains are pillared by the bipyrazolato spacers within 2D slabs extending along the (01−1) plane. Within the slabs, rectangular meshes can be appreciated: the longer edges are defined by the H_2BPZ spacers and the shorter ones by *long* Cd···Cd vectors (5.00 Å), doubly bridged by the anions. The overall structure is further strengthened by hydrogen-bonding interactions between the uncoordinated O atoms of the counterions and the N−H groups of the H_2BPZ ligands.

Passing from **8** to **9**, an increase in the M···M bridged distance is observed (see captions to Figures 4 and 5) and can be attributed not only to longer M−N bond distances but also, to a limited extent, to the different conformations of the H_2BPZ spacer, showing markedly different ϕ values (53.3° in **8** vs 0° in **9**).

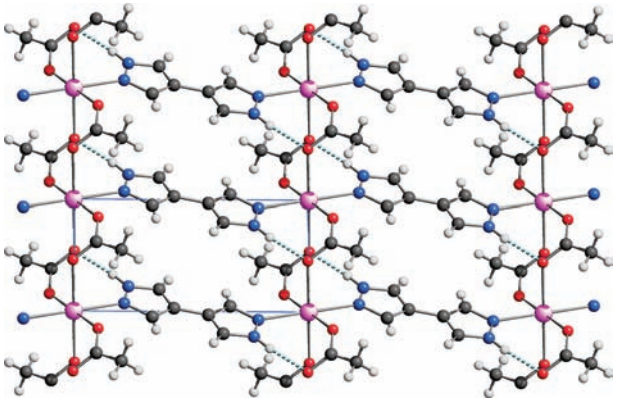

Figure 5. Portion of the crystal packing of species **9**, $[Cd(H_2BPZ)(CH_3COO)_2]$, viewed down [010]. The horizontal axis is *c*. Color code: Cd, purple; N, blue; O, red; C, gray; H, light gray. The hydrogen-bonding interactions between the unbound O atoms of the counterions and the NH groups of the ligands are depicted with fragmented lines. Significant bond distances (Å) and angles (deg): Cd−N, 2.314(9); Cd−O, 2.30(2); H_2BPZ-bridged Cd···Cd 10.3835(6); acetate-bridged Cd···Cd 4.9971(3); O···NH, 2.77(2); N−Cd−O, 86.3(6), 89.6(6), 90.4(6), 93.7(6); O−Cd−O, 88.7(6), 91.3(6).

3.5. Thermal Behavior of the BPZ-Containing Species 1−7. TGA of species **1**−**9** were performed in order to assess the thermal behavior of the synthesized materials. The acquired TGA traces are collected in Figure 6.

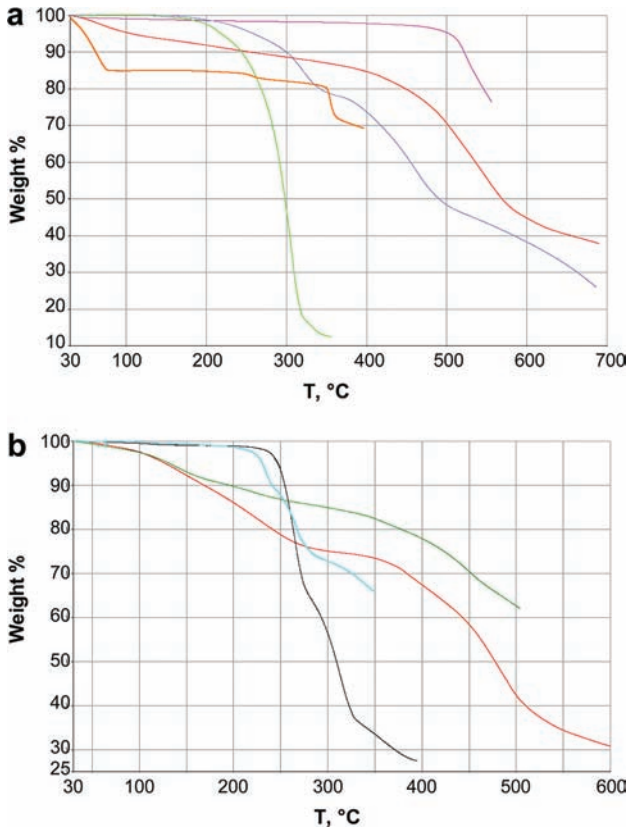

Figure 6. TGA traces of (a) species **1** (pink), **2**, (red), **3** (blue) **4**, (light green), and **5** (orange) and of (b) species **6** (red), **7** (dark green), **8** (cyan), and **9** (black).

Compound **1** shows the greatest thermal stability, remaining unaltered up to ca. 450 °C, the temperature at which a progressive decomposition begins. This behavior confirms both the absence of solvent molecules trapped in the square channels and the thermal inertness imparted to the whole material by the strong metal−pyrazolato links. This is particularly relevant for redox-inactive metal ions, as was already witnessed by the [Zn(BDP)] homologue, stable in air above 400 °C.[17d] At variance, upon heating, the cobalt-containing species **2** shows two consecutive solvent losses of about 5% each, in the temperature ranges 30−100 and 100−270 °C, respectively, likely due to the removal of water molecules adsorbed from moisture. The presence of included water molecules, apparently in contrast with the results of elemental analyses carried out on fresh specimens, should not be a surprise. As a matter of fact, **2** shows a certain tendency to adsorb aerial water: in the IR spectrum of thermally evacuated batches, afterward left in air a few hours, bands attributable to water are always detected in the region 3400−3200 cm^{-1}. Thermal decomposition of **2** starts at 320 °C. Upon an increase in the temperature, the cadmium-containing material **3** undergoes a weight loss of about 22.5% in the temperature range 290−330 °C, which can

dx.doi.org/10.1021/ic3001416 | *Inorg. Chem.* 2012, 51, 5235−5245

be interpreted as the complete removal of the DMF molecules hosted in the crystal structure (theoretical value 22.7%). This event is followed by the decomposition process, starting slightly above 350 °C. The TGA trace of **5** shows an immediate weight loss of ca. 15.1% in the temperature range 30−80 °C, which can be ascribed to the partial evolution of the low-boiling-point chlatrated solvent (theoretical value for the removal of all of the included acetonitrile molecules 17.3%). A small percentage of the bound solvent is still present at 220 °C, when a second weight loss of ca. 2.5% is observed. The evacuated material starts to decompose at 350 °C. Upon heating, the nickel-containing species **6** shows a progressive weight loss of about 22% in the 50−270 °C range, corresponding to removal of the CH_3CN molecules occupying the rhombic channels (17.7% theoretical loss for 1:1 Ni/CH_3CN stoichiometry). The TGA trace of the palladium(II) derivative **7** shows two consecutive weight losses of about 13% in the temperature range 50−250 °C, compatible with the evolution of two water molecules *per* formula unit. The presence of a higher number of water molecules than those detected by elemental analysis on a freshly prepared batch is attributed to its high hygroscopicity: repeatedly, in the IR spectra of thermally evacuated batches successively left in air for a few hours, some bands appear in the region 3400−3200 cm^{-1}, which can be confidently attributed to water adsorbed from moisture. The decomposition process starts around 280 °C. Finally, species **4** appears to be the least stable BPZ derivative. Its thermal treatment induces its decomposition already at 160 °C without previous thermal events.

In the case of the crystalline species **1**−**3**, **5**, and **6**, TGA were complemented by XRPD acquisitions performed during in situ heating−cooling cycles. These experiments aimed at verifying that the materials (i) possess permanent porosity (i.e., they do preserve their structural features upon modification of the temperature) and (ii) retain their permanent porosity along consecutive temperature cycles. As a representative example, the thermodiffractogram of **1** is reported in Figure 7. All of the other thermodiffractograms and graphical representations of the parametric treatment of the data are reported in the Supporting Information (Figures S3−S5). The zinc(II) and cobalt(II) derivatives, isolated without a clathrated solvent, where monitored with steps of 20 °C in the 30−130 °C temperature range, to allow the complete evacuation of the water molecules possibly derived from aerial moisture. Upon an increase in the temperature, both materials retain their structural features. This robustness was further verified along consecutive heating−cooling cycles, not only in the range 30−130 °C (Figures 7 and S3 in the Supporting Information) but also in the wider range of 30−200 °C (with 200 °C being the temperature of activation before the adsorption measurements; Figure S4 in the Supporting Information). As was already observed in the case of [Zn(BDP)],[17d] possessing the same structural topology, the TXRPD traces of **1** and **2** also show an extreme structural rigidity: the parametric data treatment for species **1**[26] revealed that heating up to 130 °C implies a negligible unit cell shrinkage of less than 0.1% (Figure S5 in the Supporting Information). The cadmium(II), nickel(II), and copper(II) derivatives, isolated with occluded solvent (either DMF or acetonitrile), were monitored in a higher temperature range (30−240 °C for **3** and 30−210 °C for **5** and **6**) to permit to obtain completely evacuated materials. **5** and **6** do not collapse upon solvent loss, also after repeated heating−cooling cycles. Moreover, they show a certain flexibility upon increasing (or decreasing) temperature (Figure S3 in the Supporting Information). As was already observed with [Ni(BDP)],[17d] they may exist in either closed- or open-pore forms, in which the rhombic channels possess a different cross section, depending on the external stimulus. In the case of **5**, raising the temperature up to 210 °C implies a moderate increase of all of the crystallographic axes (of 0.9, 0.8, and 1.6% for *a*−*c*, respectively), resulting in an overall increase of the unit cell volume of about 3.4% (Figure S5 in the Supporting Information). In the case of **6**, upon heating to 210 °C, *a* and *b* undergo moderate variation (increasing and decreasing about 1.7%, respectively; Figure S5 in the Supporting Information), while *c* decreases of about 4%, implying a shrinkage of similar entity of the unit cell volume. On the whole, for both materials, upon modification of the temperature, the rhombic pores behave like an accordion, as was already documented for the renowned MIL-53 family.[13]

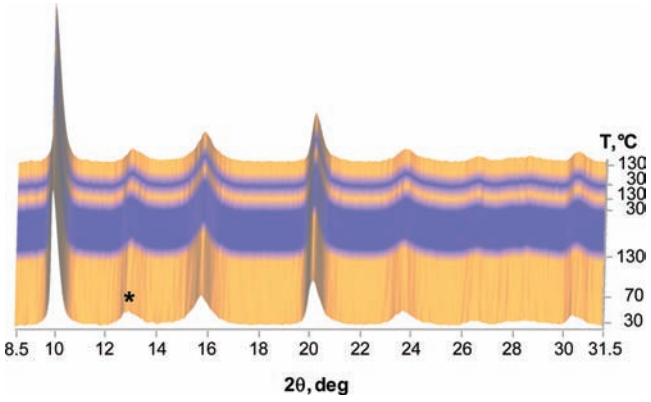

Figure 7. Plot of the XRPD patterns measured on **1** as a function of the temperature during heating in the range 30−130 °C, followed by two rapid heating−cooling cycles within the same temperature limits. The permanent porosity and rigidity of species **1** can be appreciated. Heating step: orange. Cooling step: blue. The asterisk denotes an impurity.

As for **3**, increasing the temperature brings about solvent elimination starting from 180 °C (Figure S3 in the Supporting Information): two phases, possessing the same structural topology of the parent material but with different degree of solvation, coexist up to 240 °C. Overall, solvent loss is responsible for a decrease of *a*, while *c*, along which the Cd_n helices run, remains practically undisturbed (Figure S5 in the Supporting Information): the unit cell volume of the more evacuated phase shrinks about 5%. Unfortunately, cooling the material to room temperature implies a significant loss of crystallinity, which is not recovered by annealing again at 240 °C or by contact with DMF.

Overall, the TXRPD measurements highlighted that all of the studied materials (i) are thermally stable, as was already demonstrated by TGA, (ii) possess permanent porosity, and (iii) excluding the cadmium(II) derivative, preserve their thermal robustness along with their framework topology during consecutive heating−cooling cycles. Ascertaining their permanent porosity allows to rule out that the adsorption performances observed (see below) are due exclusively to mesoporosity derived from interparticle voids. Moreover, on the basis of their stability toward repeated heating−cooling cycles, it is reasonable to assume that also their adsorption

dx.doi.org/10.1021/ic3001416 | *Inorg. Chem.* 2012, 51, 5235−5245

performances are maintained along consecutive cycles of thermal activation followed by adsorption.

3.6. Thermal Behavior of the H_2BPZ-Containing Species 8–9. Species **8** and **9** contain neutral exo-bidentate H_2BPZ spacers whose Lewis basicity is lower than that of the dianionic exo-tetradentate counterparts and whose elimination might, hence, occur at relatively low temperatures. This is indeed observed for species **8**, which loses ca. 28% of its weight in the temperature range 200–250 °C (theoretical value 29%). This event is immediately followed by further decomposition steps. On the contrary, the TGA trace of species **9** is characterized by a weight loss of 33% in the temperature range 230–250 °C, which is compatible with the evolution of acetic acid (calculated value 33%), after proton transfer from the organic ligand. The latter is possibly favored by the presence, in the crystal structure of **9**, of hydrogen-bonding interactions of the type O···H–N, between the anions and the N–H groups of the ligands (see section 3.4 and Figure 5). In this case too, this event is partially superimposed to further decomposition steps, witnessed by a smoothly changing TGA curve with poorly defined inflection points.

3.7. Gas Sorption Properties. The permanent porosity of the species **1**–**7** was probed by N_2 adsorption measurements at 77 K (Table 2). Prior to adsorption, the materials were outgassed, as detailed in the Experimental Section. The mercury(II) derivative **4** does not show any permanent porosity. On the contrary, all of the other tested materials exhibit type I adsorption isotherms with a sharp knee at low relative pressures ($p/p_0 \sim 0.01$) corresponding to the filling of the porous structure, followed by a *plateau*, suggesting that the permanent porosity of the samples is mainly composed of micropores, of quite uniform size (Figure 8). The presence of a hysteresis loop at relative pressures above 0.8 bar in the isotherms of **2**, **3**, **5**, and **6** is indicative of textural mesoporosity arising from interparticle mesopores (voids),[36] delaying gas release while passing from higher to lower relative pressures. As was already observed for [Zn(BDP)], no steps could be detected in the low-pressure region of the N_2 isotherms of **1** and **2**, at variance with what was reported for the homologous species [Co(BDP)].[17f] Fitting the N_2 isotherms gave Brunauer–Emmett–Teller (BET) specific surface areas in the range 314(2)–993(11) m^2/g and Langmuir specific surface areas in the range 509(16)–1105(1) m^2/g (see Table 2 for the actual values). Taking into consideration only the polycrystalline species, the trend shown by the values of their void volumes (**3** > **2** > **1** > **6** > **5**) is perfectly matched by those of the BET specific surface areas and of the quantity of N_2 adsorbed (Table 2).

Table 2. Synoptic Collection of the Parameters Derived from the N_2 Adsorption Isotherms at 77 K of Activated Compounds 1–3 and 5–7

	BET specific surface area (m^2/g)	Langmuir specific surface area (m^2/g)	adsorbed N_2 (cm^3/g STP)
[Zn(BPZ)], **1**	778(7)	866(1)	198.9
[Co(BPZ)], **2**	926(9)	1057(5)	242.7
[Cd(BPZ)], **3**	993(11)	1105(1)	253.9
[Cu(BPZ)], **5**	314(2)	509(16)	116.9
[Ni(BPZ)], **6**	767(4)	962(5)	221.1
[Pd(BPZ)], **7**	746(4)	1035(10)	237.6

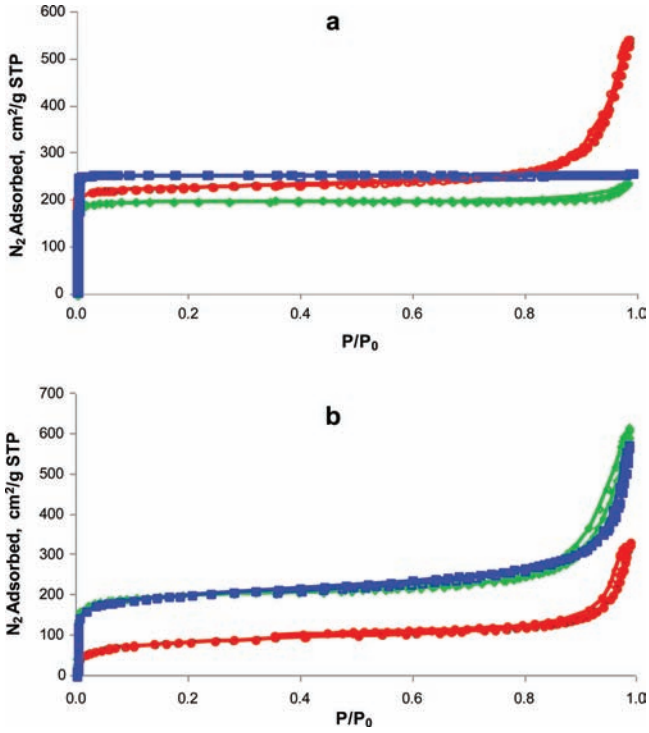

Figure 8. N_2 adsorption isotherms at 77 K for species (a) **1** (green rhombi), **2** (red circles), and **3** (blue squares) and (b) **5** (red circles), **6** (green rhombi), and **7** (blue squares). The empty symbols indicate the desorption branches.

4. CONCLUSIONS

The reaction between H_2BPZ and late-transition-metal ions, along "conventional" paths, in the presence of a deprotonating environment, or following solvothermal routes, led to the isolation of 3D PCPs of formula [M(BPZ)]·Solv (M = Zn, Co, Ni, Cu). Their specific structural motifs, retrieved by state-of-the-art XRPD methods, have been found to depend both on the stereochemistry of the metal ions and on the twist of the BPZ dianion at the C–C single bond. All of them possess a high thermal robustness, as witnessed by their stability at least up to 300 °C. Their permanent porosity, witnessed by TXRPD experiments, was essayed by N_2 adsorption measurements at 77 K, revealing quit high Langmuir specific surface areas, peaking at 1105 cm^2/g in the case of the cadmium(II) derivative. In a nondeprotonating environment, the H_2BPZ-containing derivatives **8** and **9**, featuring 2D networks, could be isolated.

The stereochemical features and the thermal robustness of the homoleptic nickel(II), copper(II), and zinc(II) polymers suggest that, once evacuated, they can be successfully used to selectively trap small molecules, aiming at efficient separation processes of gas mixtures; indeed, as was done on their larger homologues containing the bipyrazolato-1,4-benzene ligand,[17d] work can be anticipated in the direction of studying gas chromatographic separations. Finally, prompted by the results of Nomiya et al. on silver(I) imidazolate,[37] we also plan to couple the BPZ ligand with Ag^I ions, in the search for insoluble silver-containing coordination polymers capable of enhancing the well-known antifungal and antimicrobical properties of the individual (and more soluble) silver(I) salts and organic ligands.

dx.doi.org/10.1021/ic3001416 | *Inorg. Chem.* 2012, 51, 5235–5245

■ ASSOCIATED CONTENT

Supporting Information

Rietveld refinement plots, crystal data and fractional atomic coordinates, as CIF files, for species **1**−**3**, **5**, **6**, **8**, and **9**, TXRPD traces of **2**, **3**, **5**, and **6**, TXRPD traces along successive temperature cycles in the range 30−200 °C for **1** and **2**, and parametric treatment of the TXRPD data for **1**, **3**, **5**, and **6**. This material is available free of charge via the Internet at http://pubs.acs.org.

■ AUTHOR INFORMATION

Corresponding Author

*E-mail: claudio.pettinari@unicam.it (C.P.), simona.galli@uninsubria.it (S.G.).

Notes

The authors declare no competing financial interest.

■ ACKNOWLEDGMENTS

Special thanks are addressed to Dr. Ivan Timokhin and Dr. Corrado Di Nicola for sharing useful ideas. The Universities of Camerino and Insubria are acknowledged for partial funding.

■ REFERENCES

(1) Batten, S. R.; Neville, S. M.; Turner, D. R. *Coordination Polymers: Design, Analysis and Application*; Springer: New York, 2010.

(2) For example, see: Kurmoo, M. *Chem. Soc. Rev.* **2009**, *38*, 1353−1379.

(3) For example, see: (a) Lucky, M. V.; Sivakumar, S.; Reddy, M. L. P.; Paul, A. K.; Natarajan, S. *Cryst. Growth Des.* **2011**, *11*, 857−864. (b) Eryazici, I.; Farha, O. K.; Compton, O. C.; Stern, C.; Hupp, J. T.; Nguyen, S. T. *Dalton Trans.* **2011**, *40*, 9189−9193. (c) Zhao, B.; Chen, X.-Y.; Cheng, P.; Liao, D.-Z.; Yan, S.-P.; Jiang, Z.-H. *J. Am. Chem. Soc.* **2004**, *126*, 15394−15395.

(4) For example, see: Givaja, G.; Amo-Ochoa, P.; Gómez-García, C. J.; Zamora, F. *Chem. Soc. Rev.* **2011**, DOI: 10.1039/C1CS15092H.

(5) (a) Férey, G.; Serre, C.; Devic, T.; Maurin, G.; Jobic, H.; Llewellyn, P. L.; De Weireld, G.; Vimont, A.; Daturi, M.; Chang, J.-S. *Chem. Soc. Rev.* **2011**, *40*, 550−562. (b) Sculley, J.; Yuan, D.; Zhou., H.-C. *Energy Environ. Sci.* **2011**, *4*, 2721. (c) D'Alessandro, D. M.; Smit, B.; Long, J. R. *Angew. Chem., Int. Ed.* **2010**, *49*, 6058. (d) Ma, S.; Zhou, H.-C. *Chem. Commun.* **2010**, *46*, 44−53. (e) Hu, Y. H.; Zhang, L. *Adv. Mater.* **2010**, *22*, E117. (f) Murray, L. J.; Dinca, M.; Long, J. R. *Chem. Soc. Rev.* **2009**, *38*, 1294−1314. (g) Morris, R. E.; Wheatley, P. S. *Angew. Chem., Int. Ed.* **2008**, *47*, 4966−4981.

(6) For example, see: (a) Czaja, A. U.; Trukhan, N.; Muller, U. *Chem. Soc. Rev.* **2009**, *38*, 1284−1293. (b) Li, J. R.; Kuppler, R. J.; Zhou, H. C. *Chem. Soc. Rev.* **2009**, *38*, 1477−1504. (c) Liu, D.; Zhong, C. *J. Mater. Chem.* **2010**, *20*, 10308−10318.

(7) For example, see: (a) Ma, L. Q.; Abney, C.; Lin, W. B. *Chem. Soc. Rev.* **2009**, *38*, 1248−1256. (b) Lee, J.-Y.; Farha, O. K.; Roberts, J.; Scheidt, K. A.; Nguyen, S. T.; Hupp, J. T. *Chem. Soc. Rev.* **2009**, *38*, 1450−1459. (c) Farrusseng, D.; Aguado, S.; Pinel, C. *Angew. Chem., Int. Ed.* **2009**, *48*, 7502−7513.

(8) For example, see: (a) Horcajada, P.; Chalati, T.; Serre, C.; Gillet, B.; Sebrie, C.; Baati, T.; Eubank, J. F.; Heurtaux, D.; Clayette, P.; Kreuz, C.; Chang, J.-S.; Hwang, Y. K.; Marsaud, V.; Bories, P.-N.; Cynober, L.; Gil, S.; Férey, G.; Couvreur, P.; Gref, R. *Nat. Mater.* **2010**, *9*, 172. (b) Imaz, I.; Rubio-Martínez, M.; García-Fernández, L.; García, F.; Ruiz-Molina, D.; Hernando, J.; Puntes, V.; Maspoch, D. *Chem. Commun.* **2010**, *46*, 4737. (c) Ke, F.; Yuan, Y.-P.; Qiu, L.-G.; Shen, Y.-H.; Xie, A.-J.; Zhu, J.-F.; Tian, X.-Y.; Zhang, L. D. *J. Mater. Chem.* **2011**, *21*, 3843−3848.

(9) For example, see: (a) Park, K. S.; Ni, Z.; Côté, A. P.; Choi, J. Y.; Huang, R.; Uribe-Romo, F. J.; Chae, H. K.; O'Keeffe, M.; Yaghi, O. M. *Proc. Natl. Acad. Sci. U.S.A.* **2006**, *103*, 10186−10191. (b) Mathivathani Kandiah, M.; Nilsen, M. H.; Usseglio, S.; Jakobsen, S.; Olsbye, U.; Tilset, M.; Larabi, C.; Quadrelli, E. A.; Bonino, F.; Lillerud, K. P. *Chem. Mater.* **2010**, *22*, 6632−6640.

(10) For example, see: (a) Wang, Z.; Cohen, S. M. *Chem. Soc. Rev.* **2009**, *38*, 1315−1329. (b) Tanabe, K. K.; Cohen, S. M. *Chem. Soc. Rev.* **2011**, *40*, 498−519.

(11) Rosi, N. L.; Eckert, J.; Eddaoudi, M.; Vodak, D. T.; Kim, J.; O'Keeffe, M.; Yaghi, O. M. *Science* **2003**, *300*, 1127−1129.

(12) Chae, H. K.; Siberio-Pérez, D. Y.; Kim, J.; Go, Y.; Eddaoudi, M.; Matzger, A. J.; O'Keeffe, M.; Yaghi, O. M. *Nature* **2003**, *427*, 523−527.

(13) Serre, C.; Millange, F.; Thouvenot, C.; Noguès, M.; Marsolier, G.; Louër, D.; Férey, G. *J. Am. Chem. Soc.* **2002**, *124*, 13519−13526.

(14) Latroche, M.; Surblé, S.; Serre, C.; Mellot-Draznieks, C.; Llewellyn, P. L.; Lee, J.-H.; Chang, J.-S.; Jhung, S. H.; Férey, G. *Angew. Chem., Int. Ed.* **2006**, *45*, 8227−8231.

(15) (a) Masciocchi, N.; Galli, S.; Sironi, A. In *Techniques in Inorganic Chermistry*; Fackler, J. P., Falvello, L., Eds.; CRC Press, Taylor and Francis: Boca Raton, FL, 2010. (b) For example, see: Huang, X.-C.; Lin, Y.-Y.; Zhang, J.-P.; Chen, X.-M. *Angew. Chem., Int. Ed.* **2006**, *45*, 1557−1559. (c) Tian, Y.-Q.; Zhao, Y.-M.; Chen, Z.-X.; Zhang, G.-N.; Weng, L.-H.; Zhao, D.-Y. *Chem.—Eur. J.* **2007**, *13*, 4146−4154. (d) Demessence, A.; D'Alessandro, D. M.; Foo, M. L.; Long, J. R. *J. Am. Chem. Soc.* **2009**, *131*, 8784−8786. (e) Park, K. S.; Ni, Z.; Côté, A. P.; Choi, J. Y.; Huang, R.; Uribe-Romo, F. J.; Chae, H. K.; O'Keeffe, M.; Yaghi, O. M. *Proc. Natl. Acad. Sci. U.S.A.* **2006**, *103*, 10186−10191.

(16) For example, see: (a) Greathouse, J. A.; Allendorf, M. D. *J. Am. Chem. Soc.* **2006**, *128*, 10678−10679. (b) Kaye, S. S.; Dailly, A.; Yaghi, O. M.; Long, J. R. *J. Am. Chem. Soc.* **2007**, *129*, 14176−14177. (c) Low, J. J.; Benin, A. I.; Jakubczak, P.; Abrahamian, J. F.; Faheem, S. A.; Willis, R. R. *J. Am. Chem. Soc.* **2009**, *131*, 15834−15842.

(17) (a) Zhang, J.-P.; Kitagawa, S. *J. Am. Chem. Soc.* **2008**, *130*, 907−917. (b) Choi, H. J.; Dincă, M.; Dailly, A.; Long, J. R. *Energy Environ. Sci.* **2010**, *3*, 117−123. (c) Masciocchi, N.; Galli, S.; Colombo, V.; Maspero, A.; Palmisano, G.; Seyyedi, B.; Lamberti, C.; Bordiga, S. *J. Am. Chem. Soc.* **2010**, *132*, 7902−7904. (d) Galli, S.; Masciocchi, N.; Colombo, V.; Maspero, A.; Palmisano, G.; López-Garzón, F. J.; Domingo-García, M.; Fernández-Morales, I.; Barea, E.; Navarro, J. A. R. *Chem. Mater.* **2010**, *22*, 1664−1672. (e) Colombo, V.; Galli, S.; Choi, H. J.; Han, G. D.; Maspero, A.; Palmisano, G.; Masciocchi, N.; Long, J. R. *Chem. Sci.* **2011**, *2*, 1311−1319. (f) Choi, H. J.; Dincă, M.; Long, J. R. *J. Am. Chem. Soc.* **2008**, *130*, 7848−7850.

(18) Boldog, I.; Chernega, A. N.; Sieler, J.; Domasevitch, K. V. *Inorg. Chim. Acta* **2002**, *338*, 69−77.

(19) Sun, Q.-F.; Wong, K. M.-C.; Liu, L.-X.; Huang, H.-P.; Yu, S.-Y.; Yam, V. W.-W.; Li, Y.-Z.; Pan, Y.-J.; Yu, K.-C. *Inorg. Chem.* **2008**, *47*, 2142−2154.

(20) Pettinari, C.; Masciocchi, N.; Pandolfo, L.; Pucci, D. *Chem.—Eur. J.* **2010**, *16*, 1106−1123.

(21) For example, see: Bersuker, I. B. *Electronic Structure and Properties of Transition Metal Compounds*, 2nd ed.; Wiley: New York, 2010.

(22) Coelho, A. *J. Appl. Crystallogr.* **2003**, *36*, 86−95.

(23) *TOPAS*, version 3.0; Bruker AXS: Karlsruhe, Germany, 2005.

(24) To describe the H2BPZ and BPZ moieties, the **z**-matrix formalism was used, imposing idealized bond distances and angles, as follows: C−C, C−N, N−N of the heterocyclic ring, 1.36 Å; C−C, 1.50 Å; C−H, N−H, 0.95 Å; heterocyclic ring internal bond angle, 108°.

(25) Cheary, R. W.; Coelho, A. *J. Appl. Crystallogr.* **1992**, *25*, 109−121.

(26) In the case of **2**, because of the Co−K fluorescence affecting its diffractograms, the TXRPD measurements are commented only on a qualitative basis; the Le Bail parametric treatment of the data is somehow hampered.

(27) Spectral Database for Organic Compounds, 2007, http://riodb01.ibase.aist.go.jp/sdbs/cgi-bin/cre_index.cgi.

(28) Volkov, V. S.; Evtushenko, N. P.; Yatsmirskii, K. B. *Theor. Exp. Chem.* **1973**, *9*, 214−218. Lever, A. B. P.; Mantovani, E.; Ramaswamy, B. S. *Can. J. Chem.* **1971**, *49*, 1957−1964.

(29) Alvariño, G. M.; Maringgele, W.; Dechert, S.; Meyer, F. *Z. Anorg. Allg. Chem.* **2007**, *633*, 214−218.

(30) Relying on the extended use of rigid bodies for the organic portion(s), they cannot afford geometrical parameters with the accuracy typical of conventional single-crystal X-ray diffraction analyses. Nevertheless, the local coordination geometry of the metal centers, the conformation of the ligands, and the inter- or supramolecular features can be safely derived, providing relevant, otherwise inaccessible, structural information.
(31) Eddaoudi, M.; Kim, J.; Rosi, N.; Vodak, D.; Watcher, J.; O'Keeffe, M.; Yaghi, O. M. *Science* **2002**, *295*, 469−472.
(32) The void volume was estimated for desolvated crystal structures ideally maintaining the lattice metrics of the pristine materials.
(33) Dincă, M.; Yu, A. F.; Long, J. R. *J. Am. Chem. Soc.* **2006**, *128*, 8904.
(34) Demessence, A.; Long, J. R. *Chem.—Eur. J.* **2010**, *16*, 5902−5908.
(35) Because the synthetic method we adopted is not enantioselective, a conglomerate of enantiomorphic crystals (not a racemate) belonging to the enantiomorphic space groups $P6_122$ and $P6_522$ was isolated. Notably, even if a 100% pure enantiomorphic sample is available, its handiness cannot be determined by means of XRPD, with the (*hkl*) and (−*h*−*k*−*l*) Bragg reflections of the two space groups occurring at the same 2θ value.
(36) Rouquerol, F.; Rouquerol, J.; Singh, K. S. S. *Adsorption by powders and porous solids*; Academic Press: New York, 1999.
(37) Nomiya, K.; Tsuda, K.; Sudoh, T.; Oda, M. *J. Inorg. Biochem.* **1997**, *68*, 39−44.

dx.doi.org/10.1021/ic3001416 | *Inorg. Chem.* 2012, 51, 5235−5245